Erschienen in: Nature Physics ; 15 (2019), 9. - S. 960-966
https://dx.doi.org/10.1038/s41567-019-0560-2

Subcycle squeezing of light from a time flow perspective

Matthias Kizmann[1], Thiago Lucena de M. Guedes[1], Denis V. Seletskiy[1,2], Andrey S. Moskalenko[1,3*], Alfred Leitenstorfer[1] and Guido Burkard[1*]

Light as a carrier of information and energy plays a fundamental role in both general relativity and quantum physics, linking these areas that are still not fully compliant with each other. Usually the quantum nature of light is described in the frequency domain. Even for broadband quantum states with a well-defined carrier frequency, a quasi-continuous-wave picture is still applicable. However, recent access to subcycle quantum features of electromagnetic radiation promises a new class of time-dependent quantum states of light. Paralleled with the developments in attosecond science, these advances motivate an urgent need for a theoretical framework that treats arbitrary wavepackets of quantum light intrinsically in the time domain. Here, we formulate a consistent time-domain theory of the generation and sampling of few-cycle and subcycle pulsed squeezed states, leading to a relativistic interpretation in terms of induced changes in the local flow of time. Our theory enables the use of such states as a resource for novel ultrafast applications in quantum optics and quantum information.

The quantum nature and spatio-temporal structure of light are exploited in many intriguing applications ranging from novel spectroscopy methods of complex many-body phenomena[1] to quantum information processing[2–4] and subwavelength lithography[5,6]. In conventional optics, there was no control over the absolute phase of a light pulse with respect to its envelope. This situation changed abruptly with the advent of femtosecond-frequency combs[7,8]. The carrier-envelope phase is especially relevant for few-cycle pulses, which are at the heart of attosecond technology and extreme nonlinear optics[9–11]. So far, this area has exploited coherent states of light, which come closest to the classical picture of an electromagnetic field with well-defined amplitude and phase. Only recently, quantum optics was carried to an analogous level with subcycle analysis of the noise properties of infrared electric fields by electro-optic sampling with femtosecond laser pulses[12–16]. Here, the concept of a carrier-envelope phase loses its meaning because highly non-classical states of light may exhibit excessive phase fluctuations or no well-defined phase at all. Instead, it is the relative timing of a quantum noise pattern with respect to a subcycle probe that gains relevance. Interesting and unexpected phenomena may arise when the physics of such synchronal states of light is explored on a subcycle scale.

One of the most fundamental non-classical states of light is the squeezed vacuum[17–19], which enables sensitivity below the shot-noise limit in an interferometer[20–22], and can potentially improve[23,24] the metrology of gravitational waves[25]. Stationary squeezed vacuum states carry a persisting flux of photons[26], whereas there is a finite number of photons contained in a pulsed state. Pulsed squeezed light[27] with many optical oscillation cycles was realized on the basis of parametric downconversion[28]. The case of the generation of pulsed broadband ultrashort squeezing[29–31] was analysed in terms of a large set of single-frequency or broadband shaped temporal modes[29,32–34], where each mode is characterized separately. The alternative time-domain approach based on electro-optic sampling provided the first insights into the temporally resolved dynamics of few-cycle squeezing supported by a simplified theoretical description[15]. This theory was restricted to the low squeezing regime or selected points in time. Furthermore, it has not yet incorporated a finite probe pulse duration for the detection of the temporal quantum noise patterns. Here, we present methods that overcome these limitations by considering extremely short (in terms of optical cycles) pulses of squeezed vacuum light and provide a general theoretical picture of their generation and subcycle-resolved detection. We predict that the expected asymmetry between the anti-squeezed and squeezed temporal noise, well known in conventional quantum optics, can in fact be reversed for ultrabroadband driving fields, which are also within reach of state-of-the-art experiments. Our results shed light on the interplay between the quantum nature of electromagnetic fields and general relativity, leading to creation of particles out of vacuum on ultrashort timescales.

We consider the set-up depicted schematically in Fig. 1a. A coherent mid-infrared (MIR) electric driving field with a classical amplitude $\mathcal{E}(z,t)$ propagates along the z axis and is polarized along the x axis. It enters a thin transparent optical generation crystal (GX), of length l and centred at $z=0$, with a non-vanishing second-order nonlinearity $\chi^{(2)}$. Far from material resonances, $\chi^{(2)}$ can be treated as a dispersionless tensor, which in the simplest case is reducible to a single effective nonlinear coefficient d. Inside the GX, $\mathcal{E}(z,t)$ interacts with the co-propagating quantum electric field component $\hat{\varepsilon}(z,t)$, which is polarized along the y axis, belongs to the same frequency range and corresponds to the vacuum field when entering the crystal (there are no incoming photons with y polarization). This gives rise to the y component of the nonlinear polarization $\hat{P}^{(2)}(z,t)=-\varepsilon_0 d\mathcal{E}(z,t)\hat{\varepsilon}(z,t)$, where ε_0 denotes the vacuum permittivity, but generates no x component. Such a situation can be realized for various nonlinear crystals (for example, for ZnTe in a configuration where the present unit vectors $\mathbf{e}_x$ and $\mathbf{e}_z$ would be aligned along the [001] and [110] crystallographic directions, respectively[35]). The driving field is assumed to be external but the situation is similar if this field is generated in the same crystal[15].

[1]Department of Physics and Center for Applied Photonics, University of Konstanz, Konstanz, Germany. [2]Department of Engineering Physics, Polytechnique Montréal, Montréal, Québec, Canada. [3]Department of Physics, KAIST, Daejeon, Republic of Korea. *e-mail: andrey.moskalenko@uni-konstanz.de; guido.burkard@uni-konstanz.de

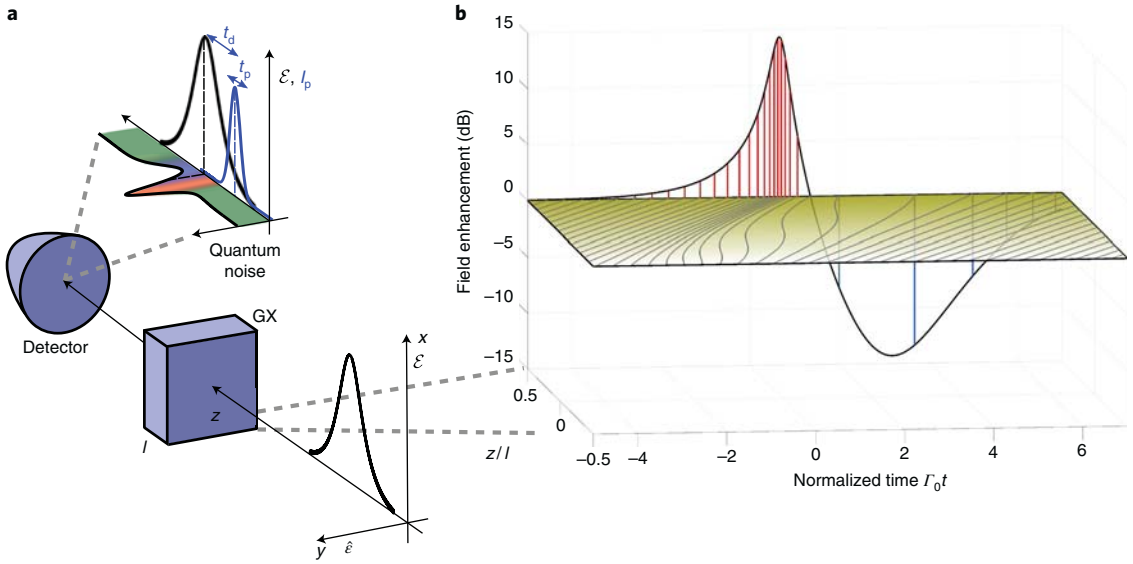

Fig. 1 | Scheme of the generation and detection set-up and the corresponding evolution of the MIR quantum field $\hat{\varepsilon}(z,t)$ inside the nonlinear crystal for a half-cycle MIR driving field with effective squeezing strength $r=5$. a, A strong MIR coherent field $\mathcal{E}(z,t)$ polarized along the x direction is sent into the nonlinear GX of length l where it squeezes the co-propagating vacuum field $\hat{\varepsilon}(z,t)$. The quantum noise of the squeezed vacuum field is shown in the horizontal plane above the detector (green represents vacuum noise, red represents anti-squeezing and blue represents squeezing). The squeezed vacuum field is then detected using electro-optic sampling: a probe pulse polarized along the x direction with intensity envelope I_p plays the role of a temporal gating applied at various time points t_d. Statistical readout allows one to obtain the time-resolved variance of $\hat{\varepsilon}(z,t)$. Subcycle resolution is achieved for sufficiently short probe pulse durations t_p. **b**, Horizontal plane: grey lines depict the world lines for $\hat{\varepsilon}(z,t)$ (determined by $\tau(z,t)=\text{const}$, characteristic curves of equation (2)), shown for the case of a half-cycle driving field (7) with duration Γ_0^{-1}. The equidistant spacing of the lines at the entrance is distorted as the quantum light propagates through the crystal. Vertical plane: field enhancement at the crystal exit is shown together with the final spacing between the world lines. In the simplified picture, red (blue) lines correspond to anti-squeezing (squeezing).

The nonlinear polarization $\hat{P}^{(2)}(z,t)$ provides a source term in the inhomogeneous wave equation for $\hat{\varepsilon}(z,t)$: $\left[\frac{\partial^2}{\partial z^2}-\frac{n^2}{c_0^2}\frac{\partial^2}{\partial t^2}\right]\hat{\varepsilon}(z,t)=\frac{1}{\varepsilon_0 c_0^2}\frac{\partial^2}{\partial t^2}\hat{P}^{(2)}(z,t)$, where c_0 and n denote the vacuum speed of light and refractive index. We decompose $\hat{\varepsilon}(z,t)=\int_{-\infty}^{\infty}\mathrm{d}\Omega\ \hat{\varepsilon}(z;\Omega)\mathrm{e}^{i(k_\Omega z-\Omega t)}$ and similarly $\mathcal{E}(z,t)$ and $\hat{P}^{(2)}(z,t)$ into plane waves[36], assuming an almost ideally linear dispersion $k_\Omega=\frac{n}{c_0}\Omega$. Here $\hat{\varepsilon}(z;\Omega)=\hat{\varepsilon}^{\dagger}(z;-\Omega)$ since the field is Hermitian. In the resulting frequency-domain integro-differential equation, we assume that $\frac{\partial^2\hat{\varepsilon}(z;\Omega)}{\partial z^2}$ can be neglected in comparison with $k_\Omega\frac{\partial\hat{\varepsilon}(z;\Omega)}{\partial z}$, as for the slowly varying amplitude approximation (SVAA)[36,37]. This leads to

$$\frac{\partial\hat{\varepsilon}(z;\Omega)}{\partial z}=-\frac{i d\Omega}{nc_0}\int_{-\infty}^{\infty}\mathrm{d}\Omega_1\,\mathcal{E}^{*}(z;\Omega_1-\Omega)\hat{\varepsilon}(z;\Omega_1) \qquad (1)$$

Integration over positive frequencies incorporates frequency-conversion processes, while integration over negative frequencies, with $\hat{\varepsilon}(z;\Omega)=\hat{\varepsilon}^{\dagger}(z;-\Omega)$, reflects parametric downconversion processes[32]. Note that the assumption of a linear dispersion relation ensures perfect phase-matching[37] for the co-propagating waves. Most importantly, it prevents the distortion of the pulse shape[38] inside the GX. This approximation works well if the GX is thin enough and the dispersion nonlinearity is negligible in the relevant frequency range. For the following discussion of ultrabroadband MIR fields with ZnTe as a typical nonlinear material, our estimations show that the GX should be thinner than 10–15 µm. However, the description of the generation process is quite general and may be applicable to other frequency ranges and appropriate nonlinear crystals[16,39,40]. The perfect phase-matching also constitutes the major difference to descriptions of conventional parametric downconversion set-ups commonly used for generation of squeezed vacuum states and entangled photon pairs[1,32]. The corresponding bandwidth-limiting factor is absent in equation (1). The spatial (angular) separation of the outgoing photons may be neglected. All emitted photons propagate in the z direction.

Transforming equation (1) back into the time domain, by integrating on the left-hand side $\int_{-\infty}^{\infty}\mathrm{d}\Omega\ \frac{\partial\hat{\varepsilon}(z;\Omega)}{\partial z}\mathrm{e}^{i(k_\Omega z-\Omega t)}=\frac{\partial\hat{\varepsilon}(z,t)}{\partial z}+\frac{n}{c_0}\frac{\partial\hat{\varepsilon}(z,t)}{\partial t}$ and using on its right-hand side the properties of the Fourier transform concerning products and derivatives, we obtain

$$\frac{\partial\hat{\varepsilon}}{\partial z}=\frac{d}{nc_0}\left[\frac{\partial\mathcal{E}}{\partial t}\hat{\varepsilon}+\left(\mathcal{E}-\frac{n^2}{d}\right)\frac{\partial\hat{\varepsilon}}{\partial t}\right] \qquad (2)$$

Note that, as a result, no central frequency and corresponding amplitude or envelope[38] were introduced in the time domain, in contrast to the conventional SVAA[37,41,42]. Therefore, also few-cycle and subcycle fields without unambiguously defined carrier frequency and phase can be described by this approach. Essentially, the way to obtain equation (2) may be considered as a broadband version of the SVAA[36] (its limits of validity are discussed in the Supplementary Information).

Equation (2) can be solved analytically by using the method of characteristics, according to which the initial conditions of the partial differential equation of interest are propagated along characteristic curves (see Methods for mathematical details). To give a physical interpretation, it is insightful to realize that there are gravitational analogues of these curves termed world lines[43]. The analogy is based on the fact that the light-driven time dependence of the refractive index, leading to nonlinear optical effects, has a closely related counterpart in general relativity[43,44]. With the ansatz $\hat{\varepsilon}(z,t)=\hat{A}(z,t)\exp[i\phi(z,t)]$, with ϕ changing in space and time

Table 1 | Comparison between the physically analogue frameworks nonlinear (quantum) optics and general relativity

Nonlinear (quantum) optics	General relativity
Driving field $\mathcal{E}$ changes the effective refractive index, $n_{\text{eff}}^2 = n^2 - 2d\mathcal{E}$	Massive/energetic bodies deform space-time, thus changing the metric $g_{\mu\nu}$ (see equation (4))
Excitations of the field modes propagate/evolve along characteristic lines	Point-like bodies/particles move along world lines
Time-dependent refractive index induces creation of photons in previously unoccupied modes	Time-dependent metric leads to particle creation even in vacuum

faster than $\hat{A}$, it is possible to rewrite either the mentioned inhomogeneous wave equation or equation (2) directly in terms of $k \equiv \nabla\phi$ and $\omega \equiv -\partial\phi/\partial t$. Separating terms that scale with different powers of the wavelength, to the lowest order in $d\mathcal{E}$, we obtain the same dispersion relation in both cases:

$$k^2 - \left[\frac{n^2}{c_0^2} - \frac{2d\mathcal{E}}{c_0^2}\right]\omega^2 = 0 \tag{3}$$

In general relativity, the dispersion relation is given by the light cone equation $g^{\mu\nu}k_\mu k_\nu = 0$, where $k_\mu = (\omega/c_0, -k)$ is the four-momentum vector. This means that the metric tensor $g_{\mu\nu}$ can be extracted from equation (3), resulting (for the '1 + 1' space-time) in the interval

$$\mathrm{d}s^2 = g_{\mu\nu}\mathrm{d}x^\mu \mathrm{d}x^\nu = \frac{c_0^2}{n^2 - 2d\mathcal{E}}\mathrm{d}t^2 - \mathrm{d}z^2 \tag{4}$$

The world lines for the evolution of $\hat{\varepsilon}$ in the crystal with a refractive index modulated by $\mathcal{E}$ can be calculated with the help of the null geodesic equations[43] coinciding in their form with the equations for the characteristic curves. We summarize the conceptual correspondence between nonlinear (quantum) optics and general relativity in Table 1.

Each world line $z(t; t_0)$ can be uniquely represented via the corresponding implicit equation $\tau(z, t) = t_0$ with its own constant t_0. Specifically, at the crystal entrance, $z = -l/2$, we have $\tau(-l/2, t) = t = t_0$. The change of the density of the world lines on propagation through the crystal at each fixed spatial position z (see Fig. 1b) determines the resulting difference in the flow of the local time $\tau(z, t)$ with respect to the laboratory time t. Note that $\tau(z, t)$ monotonically increases with t. Such a reparametrization of time can be formally introduced in connection with a conformal mapping $x^\mu \to x'^\mu$ (that is, a transformation preserving orientation and angles locally, particularly the shape of the light cones) (see Supplementary Information). The existence of such a mapping as well as a similar reparametrization of time used in cosmology, when transforming between a curved and a flat (Minkowski) metric[45], suggests terming $\tau(z, t)$ as conformal time.

Denoting the quantum field at the entrance of the generation crystal as $\hat{\varepsilon}_{\text{in}}(t) \equiv \hat{\varepsilon}(z = -l/2, t)$, the solution of equation (2) can be found as

$$\hat{\varepsilon}(z, t) = \frac{\partial\tau(z, t)}{\partial t}\hat{\varepsilon}_{\text{in}}(\tau(z, t)) \tag{5}$$

Note that back in the frequency domain, equation (5) represents a broadband (position-dependent) Bogoliubov transformation for the creation and annihilation operators:

$$\hat{a}(z; \Omega) = \int_0^\infty \mathrm{d}\Omega' p_z(\Omega, \Omega')\hat{a}_{\text{in}}(\Omega') + \int_0^\infty \mathrm{d}\Omega' q_z(\Omega, \Omega')\hat{a}_{\text{in}}^\dagger(\Omega') \tag{6}$$

with coefficients

$$\begin{aligned} p_z(\Omega, \Omega') &= -q_z(\Omega, -\Omega') \\ &= \frac{\sqrt{|\Omega'|}}{2\pi\sqrt{|\Omega|}} \int_{-\infty}^{\infty} \mathrm{e}^{i\Omega[\tau^{-1}(z,t) - nz/c_0] - i\Omega'[t + nl/(2c_0)]}\mathrm{d}t \end{aligned}$$

where τ^{-1} denotes the inverse function of τ with respect to its second argument. For the vacuum input $\hat{\varepsilon}_{\text{in}} = \hat{\varepsilon}_{\text{vac}}$, the form of the outgoing squeezed vacuum field resulting from equation (5) at the exit of the crystal can be attributed to two different effects. First, due to the driving field $\mathcal{E}(z, t)$, the wave propagation of the incoming vacuum field inside the crystal is governed by the conformal time $\tau(z, t)$. This effect is illustrated by the world lines in the horizontal plane of Fig. 1b. Second, there is a modulation of the amplitude of the quantum field by the inverse conformal factor[45] $\frac{\partial\tau(z,t)}{\partial t}$. This factor is shown in the vertical plane of Fig. 1b at the crystal exit and is essentially related to the behaviour of $\frac{\partial\mathcal{E}(z,t)}{\partial t}$ (see ref. [15]), as discussed below. Note that the quantum field is enhanced (suppressed) in the same time segments where the density of the world lines is increased (decreased) (see vertical lines in Fig. 1b). In a simplified picture, neglecting the effect of the modified density of the world lines, the amplitude modulation of the quantum field leads to a corresponding modulation in the temporal profile of its quantum noise. The quantum fluctuations of $\hat{\varepsilon}$ are suppressed beneath the vacuum level in certain time segments while exceeding it in the neighbouring segments. Squeezing (anti-squeezing) can be connected to the deceleration (acceleration) of the local flow of the conformal time $\tau(z, t)$, determined by its derivative with respect to the laboratory time t.

For part of the discussion, it is convenient to use a retarded reference frame with $t' = t - \frac{n}{c_0}z$, $z' = z$ and $\tau'(z', t') = \tau(z, t) + \frac{nl}{2c_0}$. First we convey the essence of the effect and its detection for the case of an idealized half-cycle driving pulse; afterwards we study the single-cycle case. Figure 2a depicts the evolution of the conformal time in the retarded reference frame through the crystal resulting from a half-cycle driving field of the form (see Supplementary Information)

$$\mathcal{E}'(t') = \mathcal{E}_0 \mathrm{sech}(\Gamma_0 t') \tag{7}$$

where $\mathcal{E}_0$ is the amplitude of the field and Γ_0 determines its duration. It is useful to introduce a dimensionless parameter, $r = |\mathcal{E}_0 d|\Gamma_0 l/(nc_0) > 0$, that characterizes the effective strength of the driving inducing the squeezing, and we call it the squeezing strength. At the entrance of the crystal, the conformal time matches the laboratory time: $\tau(z = -l/2, t) = t$ and $\tau'(z' = -l/2, t') = t'$. With the interaction turned on, while the quantum field propagates through the crystal its conformal time starts to deviate from the laboratory time. Via equation (5), the conformal time directly links the squeezed vacuum field at the exit of the crystal at time t to the vacuum field at the entrance at time $\tau_{\text{out}}(t) = \tau(z = l/2, t)$ (see Fig. 2b). According to equation (5), the modification of the variance of the quantum electric field after passing the crystal is given by $(\mathrm{d}\tau_{\text{out}}/\mathrm{d}t)^2$ if considered at a fixed time moment. Experimentally, the temporal dynamics of the quantum fluctuations of the electric field as a function of the relative time delay of the probe pulse t_{d} can be traced with subcycle resolution utilizing the electro-optic sampling technique and statistical readout[12,15], performing averaging over many probe pulses. The temporal resolution and sensitivity are limited by the duration of the probe pulse t_{p} during which the information about the quantum field is collected. This is a significant aspect because, apart from the change in its amplitude, the quantum field of the incoming vacuum is effectively subjected to a modified flow of time at the crystal exit, as can be seen from equation (5). Alternatively we can say that in

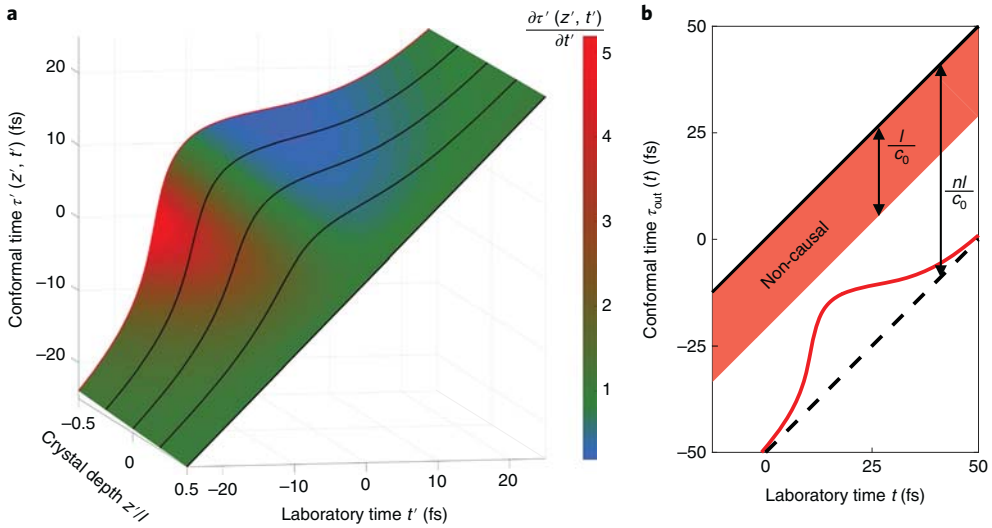

Fig. 2 | Behaviour of the conformal time with respect to the laboratory time illustrated for the half-cycle pulse (see equation (7)) with $r = 5$ and $\Gamma_0/(2\pi) = 26$ THz. a, Conformal time $\tau'(z', t')$ as a function of the laboratory time t' and the propagation length inside the crystal $z' = z$. The retarded reference frame is used. $\tau'(z', t')$ coincides with t' at the entrance of the crystal $z' = -l/2$ and starts to deviate from it for $z' > -l/2$. The graph is coloured according to the values of the inverse conformal factor $\frac{\partial \tau'(z', t')}{\partial t'}$. In the simplified picture, which does not yet incorporate the detection process influenced also by the change in the local density of the world lines, departure from green towards blue (red) leads to squeezing (anti-squeezing) of the vacuum fluctuations. The black lines support visualization of the surface. **b**, Red line: final conformal time $\tau_{out}(t) = \tau(z = l/2, t)$ at the exit of the crystal as a function of the laboratory time t, shown in the original reference frame. Dashed black line: the same without the driving field—delayed by nl/c_0 with respect to t. Full black line: the run of the laboratory time t is shown for comparison. Values of $\tau_{out}(t)$ must stay below the red area defined by the delay time $t_{d,0} = l/c_0$ in order not to violate causality (see Supplementary Information).

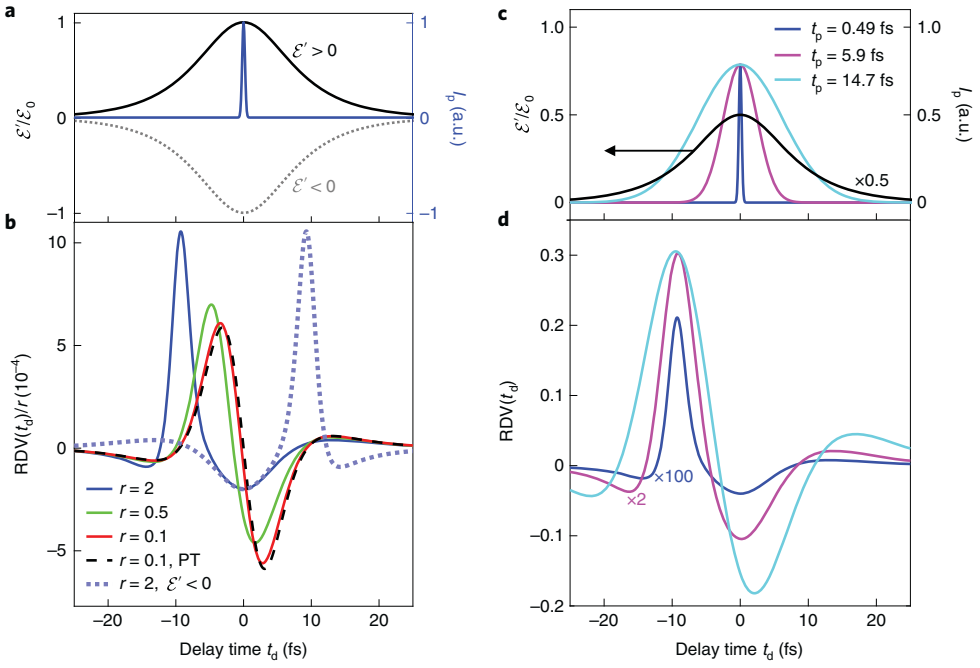

Fig. 3 | RDV as a function of the strength of the half-cycle driving field and probe pulse duration. a, Temporal profiles of the driving field $\mathcal{E}'$ with two opposite polarities and probe pulse intensity envelope I_p with duration $t_p = 0.49$ fs (blue). **b**, Dynamics of the normalized RDV for a fixed probe pulse duration $t_p = 0.49$ fs and different squeezing strengths $r = 0.1$ (red), 0.5 (green) and 2 (blue), proportional to the driving field amplitude. The normalization by r is chosen to keep the signal magnitude in the same range. For comparison, the exact analytical result within the first-order perturbation theory (PT) in r and limit of vanishing t_p is shown (black dashed line). The light blue dotted line shows the RDV for the half-cycle pulse with $\mathcal{E}' < 0$ for $r = 2$. **c**, Temporal profiles of the driving field $\mathcal{E}'$ (black, normalized by its amplitude $\mathcal{E}_0$) and probe pulse intensity envelope I_p for different probe pulse durations $t_p = 0.49$ fs (blue), 5.9 fs (magenta) and 14.7 fs (cyan) are shown on the same timescale as the RDV. **d**, Dynamics of the RDV for a fixed $r = 2$ and the same probe pulse durations as in the upper panel (note different scaling factors).

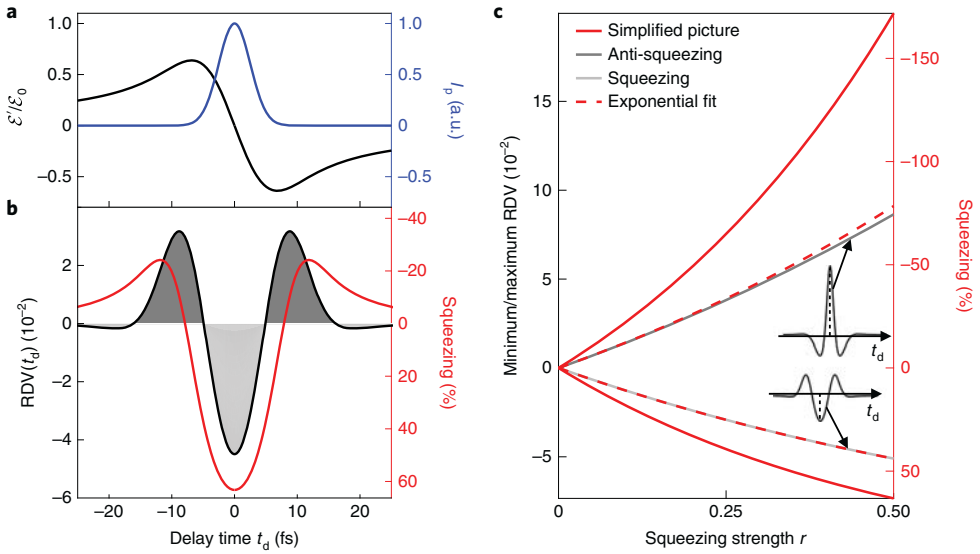

Fig. 4 | Pulsed squeezing for single-cycle driving. a, Temporal profiles of the driving field $\mathcal{E}'(t') = \mathcal{E}_0[\exp(-\Gamma_0^2 t'^2) - 1]/(\Gamma_0 t')$ with $\Gamma_0/(2\pi) = 26$ THz (black) and probe pulse intensity envelope I_p with $t_p = 5.9$ fs (blue). **b**, Corresponding dynamics of the RDV for $r = 0.5$ (black line). Dark grey (light grey) areas denote anti-squeezing (squeezing). The red line depicts the noise trace obtained within the simplified picture, where the degree of squeezing (right axis) can be extracted directly from the ratio between the variances of the squeezed and bare vacuum field at each $t_d = t$. Negative values for the degree of squeezing correspond to anti-squeezing. **c**, Values of the RDV at $t_d = 0$ fs plotted against r for two different polarities of the driving field. Depending on the polarity, it is the maximum (anti-squeezing, dark grey line, upper inset) or the minimum (squeezing, light grey line, lower inset) value of the RDV. The degree of squeezing (dashed red lines) results from an exponential fit (see Supplementary Information). The RDV in **b** is then rescaled according to this fit to obtain the degree of squeezing at arbitrary times. The red lines in **c** show the degree of squeezing calculated within the simplified picture. For a vanishing probe pulse duration $t_p \to 0$, the squeezing and anti-squeezing curves obtained from the RDV converge towards this result.

a reference frame using the conformal time $\tau_{out}(t)$ in place of the laboratory time t, the probe pulse shape and duration are modified according to the flow of $\tau_{out}(t)$ (see equation (16) in Methods). To obtain the time-resolved detected variance $V(t_d) = \langle[\hat{\varepsilon}^{(d)}_{out}(t_d)]^2\rangle$ for the outgoing quantum electric field $\hat{\varepsilon}_{out}(t) = \hat{\varepsilon}(z = l/2, t)$, that is the temporal trace of its quantum fluctuations, we employ the quantum theory of electro-optic sampling[13] (see Methods for details). We define the relative detected variance (RDV) as

$$\mathrm{RDV}(t_d) = \frac{V(t_d) - (\Delta\hat{\varepsilon}_{vac})^2}{(\Delta\hat{\varepsilon}_{vac})^2} \tag{8}$$

Here $(\Delta\hat{\varepsilon}_{vac})^2 = \langle[\hat{\varepsilon}^{(d)}_{in}]^2\rangle$ denotes the detected variance of the incoming quantum vacuum field, which does not depend on the delay time t_d.

Figure 3b depicts the RDV for the case of the half-cycle pulse equation (7), a very short detection time $t_p = 0.49$ fs and different squeezing strengths r. For $r = 0.1$, RDV(t_d) is an almost perfectly odd function (red line) with respect to the centre of the driving pulse at $t_d = 0$ fs. In this case, the temporal trace nearly coincides with the waveform proportional to the third derivative of the driving field $d^3\mathcal{E}'(t_d)/dt_d^3$ (dashed black line). This function corresponds to the exact analytic solution in the limit of small r and t_p, which can be obtained via the squeezing operator in the frequency domain (see Supplementary Information). This dynamics differs from the simplified picture where for each fixed time moment the variance of the squeezed vacuum field is determined by $[d\tau_{out}/dt]^2$ and in the low squeezing regime ($r \ll 1$) leads to temporal profiles following the first derivative $d\mathcal{E}'(t_d)/dt_d$ (ref. [15]). Note that the deviation becomes less significant if multi-cycle, more narrowband driving fields are considered.

For small r, the RDV scales linearly with r and therefore remains symmetric. A build-up of asymmetry between the time segments with reduced and excess quantum noise can be clearly observed when r is increased. First, we can see that the magnitude of the detected quantum fluctuations becomes more pronounced in the anti-squeezing period with respect to the squeezing period. This can be attributed to the fact that the conformal time $\tau_{out}(t)$ must always increase monotonically with t. As the slope of $\tau_{out}(t)$ approaches zero, the flow of time comes to a halt and, according to equation (5), $\hat{\varepsilon}_{out}(t)$ must vanish. In the simplified picture, looking only at the prefactor in equation (5), this would lead to an almost complete elimination of the quantum noise and squeezing limited by 100%. In contrast, acceleration in the flow of time in principle may lead to arbitrarily large prefactors determining the magnitude of $\hat{\varepsilon}$ in equation (5) and therefore to an arbitrarily strong enhancement of the quantum noise. In the full picture including detection, the decrease (increase) caused by the prefactor in equation (5) is partly counteracted by the slower (quicker) flow of the conformal time in $\hat{\varepsilon}_{in}(\tau_{out}(t))$ in the case of squeezing (anti-squeezing). The duration of the probe pulse seen by the incoming vacuum field thus effectively becomes smaller (larger) for squeezing (anti-squeezing) and the detected variance $V(t_d)$ increases (decreases) due to this effect[12]. Equivalently, the effect of the lower (higher) local world line densities (see Fig. 1b) alone would enhance (suppress) the detected quantum noise. Still, after the unperturbed vacuum contribution $(\Delta\hat{\varepsilon}_{vac})^2$ is subtracted in equation (5), the asymmetry in the RDV(t_d) is preserved to a large extent for sufficiently short detection times t_p. Second, with increasing r, the time segments of squeezing become broader while the time segments of anti-squeezing narrow down. This additional asymmetry can be comprehended from Fig. 2b. It is clear that the time intervals with steep slopes in the flow of the conformal time $\tau_{out}(t)$ (anti-squeezing) take less space on the horizontal axis, representing the laboratory time t, than the intervals with flat slopes (squeezing). This is what we observe for the case

of $r=2$ in Fig. 3b (blue line). Uniquely to the strong squeezing in the time domain, polarity reversal of the driving field (Fig. 3a) does not change the position of the squeezing valley while reversing the arrival time of the anti-squeezing burst.

In Fig. 3d, the dynamics of the RDV is shown for different probe pulse durations t_p and a fixed squeezing strength $r=2$. As t_p grows (see Fig. 3c), higher frequencies in $\hat{\varepsilon}_{out}(t)$ are not captured any more, leading to a flattening of the detected temporal traces. The narrow anti-squeezing peaks are affected more strongly by such changes than the valley regions of squeezing. When the probe pulse duration approaches the oscillation time of the driving field, the asymmetry is almost completely lost.

We now switch our attention to the case of a single-cycle driving pulse (Fig. 4a). Figure 4b shows the resulting dynamics of the RDV, also in terms of the degree of squeezing (see Supplementary Information). For the given amplitude of the driving field, the maximum positive degree of squeezing amounts to 49.6% while the minimum negative degree of squeezing (corresponding to anti-squeezing) constitutes only −35%. Therefore, the previously described asymmetry in favour of higher absolute values for anti-squeezing is reversed in this case. At first sight, one might wonder whether Heisenberg's uncertainty principle is violated in the described situation. Through the inspection of the RDV trace for the polarity-switched drive (inset in Fig. 4c), we discover that the amplitude of anti-squeezing is in fact nearly twice that of the squeezing (Fig. 4b). It is only in this temporally non-local sense that we are able to restore the familiar dependence of quantum noise on the squeezing strength (Fig. 4c and Supplementary Information), and hence directly recover Heisenberg's uncertainty principle.

Our work provides a consistent time-domain theory of the generation and subcycle-resolved detection of ultrabroadband waveforms of pulsed squeezed radiation, linking these processes directly to a change in the local flow of time induced by the coherent driving field. This constitutes a non-perturbative analytical solution for the operator of the generated squeezed vacuum field and the electro-optically sampled traces of its quantum noise. This solution is valid at any time and also in the high-driving regime, restricted only by conditions underlying the broadband version of the SVAA and causality. We applied our theory to predict time traces of the detected variance and corresponding degrees of squeezing belonging to ultrashort squeezed vacuum fields created by half-cycle and single-cycle driving. The results for the detected variance show that the use of electro-optic sampling for a time-resolved measurement of the noise pattern of a squeezed field inherently introduces an admixture of vacuum fluctuations. However, the asymmetries between squeezing and anti-squeezing are preserved by this measurement technique for sufficiently short probe pulses. Finally, we theoretically predict an effect that at first glance looks paradoxical: the conventionally observed asymmetry between squeezing and anti-squeezing can be reversed for specially designed driving fields.

References

1. Dorfman, K. E., Schlawin, F. & Mukamel, S. Nonlinear optical signals and spectroscopy with quantum light. *Rev. Mod. Phys.* **88**, 045008 (2016).
2. Knill, E., Laflamme, R. & Milburn, G. J. A scheme for efficient quantum computation with linear optics. *Nature* **409**, 46–52 (2001).
3. Weedbrook, C. et al. Gaussian quantum information. *Rev. Mod. Phys.* **84**, 621–669 (2012).
4. Broome, M. A. et al. Photonic boson sampling in a tunable circuit. *Science* **339**, 794–798 (2013).
5. Boto, A. N. et al. Quantum interferometric optical lithography: exploiting entanglement to beat the diffraction limit. *Phys. Rev. Lett.* **85**, 2733–2736 (2000).
6. D'Angelo, M., Chekhova, M. V. & Shih, Y. Two-photon diffraction and quantum lithography. *Phys. Rev. Lett.* **87**, 013602 (2001).
7. Jones, D. J. et al. Carrier-envelope phase control of femtosecond mode-locked lasers and direct optical frequency synthesis. *Science* **288**, 635–639 (2000).
8. Holzwarth, R. et al. Optical frequency synthesizer for precision spectroscopy. *Phys. Rev. Lett.* **85**, 2264–2267 (2000).
9. Corkum, P. B. & Krausz, F. Attosecond science. *Nat. Phys.* **3**, 381–387 (2007).
10. Krausz, F. & Ivanov, M. Attosecond physics. *Rev. Mod. Phys.* **81**, 163–234 (2009).
11. Moskalenko, A. S., Zhu, Z.-G. & Berakdar, J. Charge and spin dynamics driven by ultrashort extreme broadband pulses: a theory perspective. *Phys. Rep.* **672**, 1–82 (2017).
12. Riek, C. et al. Direct sampling of electric-field vacuum fluctuations. *Science* **350**, 420–423 (2015).
13. Moskalenko, A. S., Riek, C., Seletskiy, D. V., Burkard, G. & Leitenstorfer, A. Paraxial theory of direct electro-optic sampling of the quantum vacuum. *Phys. Rev. Lett.* **115**, 263601 (2015).
14. Benea-Chelmus, I.-C. et al. Subcycle measurement of intensity correlations in the terahertz frequency range. *Phys. Rev. A* **93**, 043812 (2016).
15. Riek, C. et al. Subcycle quantum electrodynamics. *Nature* **541**, 376–379 (2017).
16. Benea-Chelmus, I.-C., Settembrini, F. F., Scalari, G. & Faist, J. Electric field correlation measurements on the electromagnetic vacuum state. *Nature* **568**, 202–206 (2019).
17. Breitenbach, G., Schiller, S. & Mlynek, J. Measurement of the quantum states of squeezed light. *Nature* **387**, 471–475 (1997).
18. Lvovsky, A. I. in *Photonics: Scientific Foundations, Technology and Applications* Vol. 1 (ed. Andrews, D. L.) 121–163 (John Wiley & Sons, 2015).
19. Chekhova, M., Leuchs, G. & Żukowski, M. Bright squeezed vacuum: entanglement of macroscopic light beams. *Opt. Commun.* **337**, 27–43 (2015).
20. Caves, C. M. Quantum-mechanical noise in an interferometer. *Phys. Rev. D* **23**, 1693–1708 (1981).
21. Xiao, M., Wu, L.-A. & Kimble, H. J. Precision measurement beyond the shot-noise limit. *Phys. Rev. Lett.* **59**, 278–281 (1987).
22. Grangier, P., Slusher, R. E., Yurke, B. & LaPorta, A. Squeezed-light–enhanced polarization interferometer. *Phys. Rev. Lett.* **59**, 2153–2156 (1987).
23. Abadie, J. et al. A gravitational wave observatory operating beyond the quantum shot-noise limit. *Nat. Phys.* **7**, 962–965 (2011).
24. Aasi, J. et al. Enhanced sensitivity of the LIGO gravitational wave detector by using squeezed states of light. *Nat. Photon.* **7**, 613–619 (2013).
25. Abbott, B. P. et al. Observation of gravitational waves from a binary black hole merger. *Phys. Rev. Lett.* **116**, 061102 (2016).
26. Blow, K. J., Loudon, R., Phoenix, S. J. D. & Shepherd, T. J. Continuum fields in quantum optics. *Phys. Rev. A* **42**, 4102–4114 (1990).
27. Anderson, M. E., McAlister, D. F., Raymer, M. G. & Gupta, M. C. Pulsed squeezed-light generation in $\chi^{(2)}$ nonlinear waveguides. *J. Opt. Soc. Am. B* **14**, 3180–3190 (1997).
28. Slusher, R. E., Grangier, P., LaPorta, A., Yurke, B. & Potasek, M. J. Pulsed squeezed light. *Phys. Rev. Lett.* **59**, 2566–2569 (1987).
29. Wasilewski, W., Lvovsky, A. I., Banaszek, K. & Radzewicz, C. Pulsed squeezed light: simultaneous squeezing of multiple modes. *Phys. Rev. A* **73**, 063819 (2006).
30. Harris, S. E. Chirp and compress: toward single-cycle biphotons. *Phys. Rev. Lett.* **98**, 063602 (2007).
31. Horoshko, D. B. & Kolobov, M. I. Towards single-cycle squeezing in chirped quasi-phase-matched optical parametric down-conversion. *Phys. Rev. A* **88**, 033806 (2013).
32. Christ, A., Brecht, B., Mauerer, W. & Silberhorn, C. Theory of quantum frequency conversion and type-II parametric down-conversion in the high-gain regime. *New J. Phys.* **15**, 053038 (2013).
33. Shaked, Y. et al. Lifting the bandwidth limit of optical homodyne measurement with broadband parametric amplification. *Nat. Commun.* **9**, 609 (2018).
34. Sharapova, P. R., Tikhonova, O. V., Lemieux, S., Boyd, R. W. & Chekhova, M. V. Bright squeezed vacuum in a nonlinear interferometer: frequency and temporal Schmidt-mode description. *Phys. Rev. A* **97**, 053827 (2018).
35. Planken, P. C. M., Nienhuys, H.-K., Bakker, H. J. & Wenckebach, T. Measurement and calculation of the orientation dependence of terahertz pulse detection in ZnTe. *J. Opt. Soc. Am. B* **18**, 313–317 (2001).
36. Loudon, R. *The Quantum Theory of Light* (Oxford Univ. Press, 2000).
37. Boyd, R. W. *Nonlinear Optics* 3rd edn (Academic, 2008).
38. Brabec, T. & Krausz, F. Nonlinear optical pulse propagation in the single-cycle regime. *Phys. Rev. Lett.* **78**, 3282–3285 (1997).
39. Keiber, S. et al. Electro-optic sampling of near-infrared waveforms. *Nat. Photon.* **10**, 159–162 (2016).
40. Virally, S. & Reulet, B. Unidimensional time domain quantum optics. Preprint at *arXiv* https://arxiv.org/abs/1810.06932 (2018).

41. Shen, Y. R. *Principles of Nonlinear Optics* (Wiley-Interscience, 1984).
42. Powers, P. E. *Fundamentals of Nonlinear Optics* (Taylor & Francis, 2011).
43. Guedes, T. L. M. et al. Spectra of ultrabroadband squeezed pulses and the finite-time Unruh–Davies effect. *Phys. Rev. Lett.* **122**, 053604 (2019).
44. Belgiorno, F. et al. Dielectric black holes induced by a refractive index perturbation and the Hawking effect. *Phys. Rev. D* **83**, 024015 (2011).
45. Mukhanov, V. *Physical Foundations of Cosmology* (Cambridge Univ. Press, 2005).

Acknowledgements

We thank P. Sulzer and R. Haussmann for discussions. Support by the DFG via SFB767, by Baden-Württemberg Stiftung via the Elite programme for Postdocs (project 'Fundamental aspects of relativity and causality in time-resolved quantum optics') and by the Young Scholar Fund of the University of Konstanz is acknowledged. M.K. is indebted to the LGFG PhD fellowship programme of the University of Konstanz.

Author contributions

A.S.M., D.V.S. and G.B. conceived the idea. A.S.M. managed the project and supervised the research. M.K. found the exact analytical solution in the time domain, performed numerical calculations and prepared the figures. T.L.d.M.G. obtained the perturbative analytic solution via the squeezing operator in the frequency domain. M.K., T.L.d.M.G. and A.S.M. wrote the first version of the paper. D.V.S. and A.L. provided several important physical insights and interpretations. All authors discussed the results and contributed to the writing of the final manuscript.

Competing interests

The authors declare no competing interests.

Methods

Method of characteristics. The method of characteristics is used to solve a given partial differential equation (PDE) by reducing it to a set of ordinary differential equations (ODEs), which define parametric curves in the space of the PDE variables (so-called characteristic curves). These curves allow one then to construct the solution of the PDE. Let us assume that the original variables of the PDE, in our case equation (2), depend on the parameter ζ. Comparison of the total derivative of $\hat{\varepsilon}$ with respect to ζ with equation (2) gives us ODEs for $z(\zeta)$ and $t(\zeta)$ (with their respective initial conditions):

$$\frac{\mathrm{d}z}{\mathrm{d}\zeta}=1, \qquad z(\zeta=0)=-l/2 \tag{9}$$

$$\frac{\mathrm{d}t}{\mathrm{d}\zeta}=-\frac{d}{nc_0}\left[\mathcal{E}(z,t)-\frac{n^2}{d}\right]_{z=z(\zeta),t=t(\zeta)}, \qquad t(\zeta=0)=\tau \tag{10}$$

Here an additional parameter τ was introduced as the initial condition for $t(\zeta)$ when $\zeta=0$. Solving equation (9) reveals that $\zeta=z+l/2$. Changing the variable from ζ to z in equation (10) and solving it, we obtain $t(z,\tau)$, where now also an explicit dependence on τ appears. Finally, the function $t(z,\tau)$ can be inverted to obtain $\tau(z,t)$ with $\tau(z=-l/2,t)=t$. The functional form of $\tau(z,t)$ ensures that the total derivative of $\tau(z(\zeta),t(\zeta))$ with respect to ζ vanishes

$$\frac{\mathrm{d}\tau(z(\zeta),t(\zeta))}{\mathrm{d}\zeta}=\frac{\partial\tau(z,t)}{\partial z}-\frac{d}{nc_0}\left[\mathcal{E}(z,t)-\frac{n^2}{d}\right]\frac{\partial\tau(z,t)}{\partial t}=0 \tag{11}$$

meaning that $\tau(z(\zeta),t(\zeta))$ remains constant when moving along a characteristic curve $\{z(\zeta),t(\zeta)\}$ parameterized by ζ. This PDE for $\tau(z,t)$ can now be used to prove that equation (5) indeed satisfies equation (2). Therefore, the only remaining non-trivial task is to solve equation (10) finding $\tau(z,t)$. Inserting the solution for $\tau(z,t)$ into equation (5) then gives $\hat{\varepsilon}(z,t)$.

For the purpose of solving equation (10), the retarded reference frame with $t'=t-nz/c_0$, $z'=z$ and $\mathcal{E}(z,t)=\mathcal{E}'(t')$ is utilized. This transforms equation (10) into a separable ODE. $\tau(z,t)$ can then be expressed as

$$\tau(z,t)=f^{-1}\left(f\left(t-\frac{n}{c_0}z\right)+\frac{1}{nc_0}\left(z+\frac{l}{2}\right)\right)-\frac{nl}{2c_0} \tag{12}$$

in the original reference frame, where $f(t')$ is defined as the solution of the following ODE

$$\frac{\mathrm{d}f(t')}{\mathrm{d}t'}=\frac{1}{d\mathcal{E}'(t')} \tag{13}$$

Note that for equation (13) no initial condition needs to be stated because it can be chosen arbitrarily. The necessary initial condition is already incorporated in the solution for $\tau(z,t)$ with $\tau(z=-l/2,t)=t$, regardless of the specific form of $f(t')$.

Quantum electro-optic sampling. The quantum theory of electro-optic sampling[13] is employed to model the detection process. Electro-optic sampling is generally based on upconversion of the MIR (terahertz, multi-terahertz) field to the near-infrared (NIR) range. More specifically, a second-order nonlinear interaction provides mixing between the MIR field and an ultrafast gate pulse of the probe field, which is of a duration shorter than the half-cycle of the sampled field[42,46]. Scanning the relative delay t_d between the MIR field and the centre of the probe pulse allows for mapping out the temporal evolution of the MIR waveform. It is extracted from the polarization state of the NIR photons, which are absorbed and counted in a pair of fast (that is, ~1 GHz electronic bandwidth) balanced photodetectors. The technique can also be operated in the regime of statistical readout, where probability distributions based on millions of individual NIR pulses can be analysed at each temporal delay between the MIR field and the gate pulse, providing access to the temporally resolved quantum statistics of the sampled field[12,15,16].

The variance of the outgoing quantum field $\hat{\varepsilon}'_\mathrm{out}(t')$ is calculated as a function of the relative delay time t_d with respect to the centre of an ultrashort higher-frequency probe pulse $\mathcal{E}'_\mathrm{p}(t')$ (for convenience the retarded reference frame is used here). The resulting operator of the sampled field is given by

$$\hat{\varepsilon}^{(\mathrm{d})}_\mathrm{out}(t_\mathrm{d})=\int_{-\infty}^{\infty}\mathrm{d}t'\ R(t_\mathrm{d}-t')\hat{\varepsilon}'_\mathrm{out}(t') \tag{14}$$

The detector function $R(t_\mathrm{d})$ is determined by the normalized intensity of the probe field that, for a fast oscillating probe field, can be replaced by the normalized intensity envelope:

$$R(t_\mathrm{d})=\frac{|\mathcal{E}'_p(t_\mathrm{d})|^2}{\int_{-\infty}^{\infty}\mathrm{d}t'\ |\mathcal{E}'_p(t')|^2}\approx\frac{I'_p(t_\mathrm{d})}{\int_{-\infty}^{\infty}\mathrm{d}t' I'_p(t')} \tag{15}$$

Then for the outgoing quantum field, determined by equation (5) at $z=l/2$, the operator of the sampled field can be expressed via the incoming quantum field $\hat{\varepsilon}_\mathrm{in}(t)$ in the original reference frame as

$$\hat{\varepsilon}^{(\mathrm{d})}_\mathrm{out}(t_\mathrm{d})=\int_{-\infty}^{\infty}\mathrm{d}t\ R(t_\mathrm{d}-\tau^{-1}_\mathrm{out}(t))\hat{\varepsilon}_\mathrm{in}(t) \tag{16}$$

where $x=\tau^{-1}_\mathrm{out}(y)$ denotes the inverse function of $y=\tau_\mathrm{out}(x)$. Let us consider the case where the incoming field corresponds to the vacuum state. Then equation (16) shows that sampling of the generated squeezed field by the probe pulse in an inertial reference frame can be alternatively viewed as sampling of the bare vacuum field in a reference frame with a non-uniform time flow given by $\tau^{-1}_\mathrm{out}(t)$. In the latter reference frame, the shape of the used probe pulse is then effectively transformed. To characterize the dynamics of the resulting quantum fluctuations, we evaluate the RDV that is given by equation (8). For the corresponding calculations in this paper, we used a Gaussian shape of the probe intensity envelope with the full-width at half-maximum duration t_p so that $R(t_\mathrm{d})=\frac{2\sqrt{\ln 2}}{\sqrt{\pi}t_\mathrm{p}}\exp\left(-\frac{4\ln 2\, t_\mathrm{d}^2}{t_\mathrm{p}^2}\right)$.

To analyse further the quantum aspects of the generated signals in our time-resolved detection theory, it is elucidating to consider the positive $\hat{\varepsilon}'^{(+)}_\mathrm{out}(t')$ and negative $\hat{\varepsilon}'^{(-)}_\mathrm{out}(t')$ frequency parts[47] of the generated quantum field $\hat{\varepsilon}'_\mathrm{out}(t')=\hat{\varepsilon}'^{(+)}_\mathrm{out}(t')+\hat{\varepsilon}'^{(-)}_\mathrm{out}(t')$. These parts contain only annihilation or only creation operators, respectively. The sampling of the corresponding field parts, which are non-Hermitian, can be performed by combining the information on the full field itself $\hat{\varepsilon}'_\mathrm{out}(t')$ and the same field with $\pi/2$-shifted carrier-envelope phase $\hat{\varepsilon}'_{\mathrm{out},\frac{\pi}{2}}(t'):\hat{\varepsilon}'^{(\pm)}_\mathrm{out}(t')=\left[\hat{\varepsilon}'_\mathrm{out}(t')\mp i\hat{\varepsilon}'_{\mathrm{out},\frac{\pi}{2}}(t')\right]/2$. Such a phase shift can be implemented experimentally by inserting an appropriate broadband carrier-envelope phase shifter[48] or in a variation of the electro-optic detection set-up[49]. Mathematically, the corresponding operation represents the Hilbert transform[40] of the original generated field $\hat{\varepsilon}'_\mathrm{out}(t')$. In the time-resolved detection, we get

$$\hat{\varepsilon}^{(\mathrm{d})}_{\mathrm{out},\frac{\pi}{2}}(t_\mathrm{d})=\int_{-\infty}^{\infty}\mathrm{d}t'\ R(t_\mathrm{d}-t')\hat{\varepsilon}'_{\mathrm{out},\frac{\pi}{2}}(t')=\int_{-\infty}^{\infty}\mathrm{d}t'\ R_{\frac{\pi}{2}}(t_\mathrm{d}-t')\hat{\varepsilon}'_\mathrm{out}(t') \tag{17}$$

where $R_{\frac{\pi}{2}}(t)$ is obtained from $R(t)$ via the shift of the carrier-envelope phase by $\pi/2$. In the frequency domain, $R_{\frac{\pi}{2}}(\omega)=iR(\omega)$ for $\omega>0$ and $R_{\frac{\pi}{2}}(\omega)=-iR(\omega)$ for $\omega<0$. We can also express $\hat{\varepsilon}^{(\mathrm{d})}_{\mathrm{out},\frac{\pi}{2}}(t_\mathrm{d})$ via the input field $\hat{\varepsilon}_\mathrm{in}(t)$, in the same way as in equation (16). Measurements on $\hat{\varepsilon}'_\mathrm{out}(t')$ and $\hat{\varepsilon}'_{\mathrm{out},\frac{\pi}{2}}(t')$ can be performed simultaneously, in parallel, after a beamsplitter. Note that in the described detection scheme, giving local temporal access to the generated quantum field, it is more natural and advantageous to operate with $\hat{\varepsilon}'^{(-)}_\mathrm{out}(t')$ and $\hat{\varepsilon}'^{(+)}_\mathrm{out}(t')$ in place of the time-domain version of the creation $\hat{a}^\dagger(t')$ and annihilation $\hat{a}(t')$ operators, which are also possible to introduce[40]. This access enables a deeper study of the intrinsically quantum properties of the generated field. For example, taking the input vacuum field having zero intensity flux our generation process leads to the appearance of the time-dependent short-living intensity flux, which is not possible to replicate with stochastical quasi-classical models for the field. The corresponding illustration and comparison of the simultaneous temporal dynamics of the RDV for both $\hat{\varepsilon}'_\mathrm{out}(t')$ and $\hat{\varepsilon}'_{\mathrm{out},\frac{\pi}{2}}(t')$ are provided in Supplementary Information.

The calculated values of the RDV typically are small compared to the values of RDV and respective degrees of squeezing that would follow directly from the simplified picture (see Fig. 4b). The reason for this is that the RDV (see equation (8)) is defined as the relative difference between the detected variance of the generated field and that of the unperturbed vacuum fluctuations. To resolve the signal in the time domain, the probe duration has to be much shorter than the typical timescales of the signal. Thus, the frequency spectrum of the probe has to be much broader than that of the coherent field driving the squeezing. This means that the probe pulse will sample not only modes at the frequencies that are affected by the driving field but also modes at higher frequencies that remain untouched. Therefore, the contribution of the unperturbed vacuum fluctuations to the RDV has to be significantly larger than the contribution from the frequency range affected by the generation process to appropriately resolve the temporal squeezing pattern. This can be interpreted as an admixture of vacuum fluctuations to the signal that can be modelled by losses. However, it is important to note that rather than being losses that can be avoided, these losses are inherent to the measurement process and are necessary to appropriately resolve the signal in time. Nevertheless, losses do not necessarily represent an obstacle for the reconstruction of the degree of the generated squeezing[15], which is shown in Fig. 4c.

The experimental realization of quantum electro-optic sampling involves an additional contribution to the detected variance originating from the shot noise of the probe pulse. This contribution is an important issue but is tractable experimentally by referencing the signal with respect to the vacuum level. In the considered situation, this can be accomplished by producing sets of two immediately consecutive measurements with and without the squeezing process initiated in the GX crystal, respectively. Therefore, the relevant quantity measured experimentally, and connected to the calculated RDV, is the relative differential

noise (RDN)[15], incorporating the shot-noise (SN) contribution $(\Delta\mathcal{E}_{\mathrm{p,SN}})^2$. The RDN is given by

$$\mathrm{RDN}(t_\mathrm{d}) = (\sqrt{V(t_\mathrm{d})} - \Delta\hat{\varepsilon}_\mathrm{vac}) \frac{\Delta\hat{\varepsilon}_\mathrm{vac}}{(\Delta\mathcal{E}_{\mathrm{p,SN}})^2} \tag{18}$$

(see equation (8) for comparison).

The detection set-up can be operated under conditions when the probe pulse intensity is high enough so that the shot-noise equivalent field amplitude $\Delta\mathcal{E}_{\mathrm{p,SN}}$ (inversely proportional to the square root of the intensity of the probe field) is reduced to an appropriate level, which is still higher than but comparable with both the root mean square values of the detected vacuum field $\Delta\hat{\varepsilon}_\mathrm{vac}$ and the deviation induced due to the squeezing $\sqrt{V(t_\mathrm{d})} - \Delta\hat{\varepsilon}_\mathrm{vac}$. Additionally, a large enough number of repetitions (millions in practice) are required to suppress the uncertainty in the detected variances for the generated quantum field and the bare vacuum. Under such conditions, an appropriate signal-to-error ratio can be reached for the RDN. Knowing the particular relevant probe intensity determining the shot-noise level, one can straightforwardly recalculate the RDV from the RDN and vice versa.

References

46. Gallot, G. & Grischkowsky, D. Electro-optic detection of terahertz radiation. *J. Opt. Soc. Am. B* **16**, 1204–1212 (1999).
47. Glauber, R. J. The quantum theory of optical coherence. *Phys. Rev.* **130**, 2529–2539 (1963).
48. Kawada, Y., Yasuda, T. & Takahashi, H. Carrier envelope phase shifter for broadband terahertz pulses. *Opt. Lett.* **41**, 986–989 (2016).
49. Riek, C., Sulzer, P., Seeger, M., Seletskiy, D. V. & Leitenstorfer, A. Simultaneous sampling of electric field quadratures in the time domain. In *Conference on Lasers and Electro-Optics, OSA Technical Digest* paper SM1L.1 (Optical Society of America, 2016).